A Hybrid Spin-charge Mixed-mode Simulation Framework for Evaluating STT-MRAM Bit-cells Utilizing Multiferroic Tunnel Junctions

Xuanyao Fong and Kaushik Roy
School of Electrical and Computer Engineering
Purdue University
West Lafayette, Indiana 47907
Email: {xfong, kaushik}@ecn.purdue.edu

***Abstract*—Multiferroic tunnel junctions (MFTJs) consisting of ferromagnetic contacts sandwiching a ferroelectric tunnel barrier have been proposed as possible data storage elements. However, a simulation framework is needed for evaluating and analyzing the design and performance of memory cells based on MFTJs. In this paper, we propose a spin-charge mixed-mode simulation framework that captures the device physics of the MFTJ for SPICE circuit simulations.**

I. Introduction

The emergence of spin-transfer torque MRAM (STT-MRAM) as a strong candidate for future universal memory technology (due to its non-volatility, compatibility with CMOS technology, scalability and reasonably high performance [1]) has led to significant research interest. However, STT-MRAM bit-cells suffer from conflicting design requirements for reading from and writing to the cell [2]. The tunneling magnetoresistance is used for sensing data stored in STT-MRAM bit-cells. The MTJ consists of a pinned and a free magnetic layer (PL and FL, respectively) sandwiching a tunnel barrier. MTJ conductance depends on the relative magnetization of PL and FL, and is switched between high and low conductance in STT-MRAM by manipulating FL magnetization. Analysis of 1T-1MTJ STT-MRAM bit-cells show that sensing failures may severely limit the bit-cell area and failure probability [3]. Enhancing the tunneling magnetoresistance effect may improve the sensing failure probability of STT-MRAM bit-cells. Replacing the tunnel barrier in an MTJ with a ferroelectric tunnel barrier (FTB) allows modulation of the tunneling conductance through the tunneling electroresistance (*TER*) effect [4], which may be used to enhance the tunneling magnetoresistance ratio (*TMR*) of the tunnel junction (TJ) and improve sensing failures in STT-MRAM memory cells. However, a simulation framework that captures both tunneling electroresistance and tunneling magnetoresistance effects is needed to evaluate the effectiveness of magnetic ferroelectric tunnel junctions (MFTJs) on improving STT-MRAM sensing failure. This paper presents a mixed-mode simulation framework that captures both effects in the device for circuit level simulations. The rest of this paper is organized as follows. Section II describes our proposed simulation framework. The MFTJ structure analyzed using our proposed simulation framework is then presented in Section III. Finally, Section IV discusses the simulation results and Section V concludes this paper.

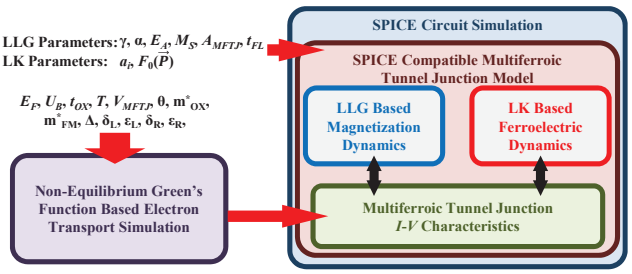

Fig. 1. Flow chart of our proposed simulation framework.

II. Proposed Simulation Framework

Our proposed simulation framework (Fig. 1) consists of 1) a Landau-Lifshitz-Gilbert (LLG) model for capturing magnetization dynamics, 2) a Landau-Khalatnikov (LK) dynamical ferroelectric model, 3) a Non-Equilibrium Green's Function (NEGF) formalism based solver for electron transport, and 4) a SPICE compatible circuit model for MFTJ.

A. Landau-Lifshitz-Gilbert (LLG) Model

Magnetization dynamics of the FL affect the MFTJ resistance (R_{MFTJ}) and needs to be modeled in order to properly describe MFTJ dynamics during switching. In scaled STT-MRAM technology, the FL can be approximated as a mono-domain magnet. Magnetization dynamics of a mono-domain magnet is obtained by solving the Landau-Lifshitz-Gilbert (LLG) equation shown as (1). γ is the gyromagnetic ratio, α is the Gilbert damping factor, $\hat{m}$ is the magnetization vector of the nano-magnet, $\vec{H}_{EFF}$ is the effective magnetic field on the nano-magnet and $\vec{STT}$ is the spin torque term which will be discussed in Section II-C.

$\vec{H}_{EFF}$ captures all magnetic-field like interactions as shown in (2). $\vec{H}_{UNI}$ is the uniaxial anisotropy field, $\vec{H}_{EXT}$ is the externally applied magnetic field, $\vec{H}_{DEMAG}$ is the demagnetization field, $\vec{H}_{DIP}$ is the dipolar field from other nano-magnets, and $\vec{H}_{TH}$ is the thermal fluctuation field. Using Cartesian coordinates, the equilibrium direction (or the easy axis) of the magnet is defined to be along the z-axis ($\hat{z}$). Thus, $\hat{m}$ is either $+\hat{z}$ or $-\hat{z}$ in equilibrium. The activation energy (E_A) is used to calculate the uniaxial anisotropy field using (3)-(4), where M_S and V are the saturation magnetization and

978-1-4673-5736-4/13/$31.00 ©2013 IEEE

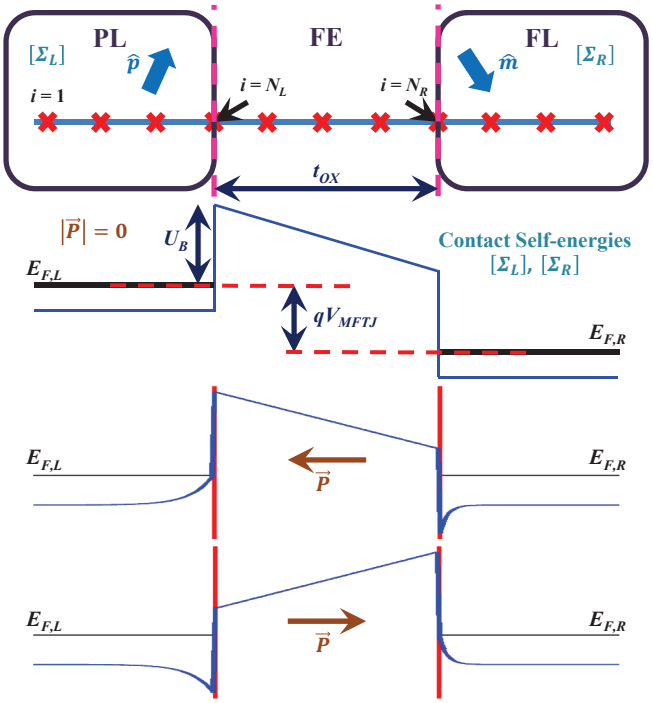

Fig. 2. Conceptual description of the MFTJ in the NEGF framework, where each cross represents a lattice point. The potential profile across the MFTJ under different FE polarizations without spin splitting are also shown.

volume of FL, respectively (and $E_A = Ku_2V$). Anisotropies of nano-magnets with in-plane anisotropy (IMA) may be modeled using (3), whereas anisotropies of nano-magnets with perpendicular magnetic anisotropy (PMA) may be modeled using (4) [5]. In an STT-MRAM array where there are many nano-magnets, the dipolar coupling between nano-magnets may be captured using (5), where for the i-th nano-magnet, $\vec{r_i}$ is the vector from the nano-magnet to FL, $\hat{m}_i$ describes its magnetization direction, and μ_r is the relative permeability of the material in which all nano-magnets and FL are buried in. Temperature effects as prescribed by Brown are captured in (6), where the components of $\vec{\xi}$ are independent Gaussian random variables. k_B is the Boltzmann constant and T is the absolute temperature.

B. Landau-Khalatnikov (LK) Model

Dynamics of ferroelectric polarization is described by the Landau-Khalatnikov equation [6] as in (7), where $F(\vec{P})$ is the free energy functional of the ferroelectric material, and a_0 is a proportionality constant. In our model, $F(\vec{P})$ is written as (8), where $F_0(\vec{P})$ describes the ferroelectric anisotropy, a_1 is a proportionality constant, and $\vec{E}$ is the external electric field applied across the ferroelectric.

C. Non-Equilibrium Green's Function (NEGF) Method

The Non-Equilibrium Green's Function (NEGF) formalism [7] is used to calculate the $I-V$ characteristic of the MFTJ, which is used in the SPICE circuit model of the MFTJ for circuit simulations. The NEGF formalism may also be used to calculate the spin torque acting on the free layer (FL) of the MFTJ when solving for the magnetization dynamics of FL.

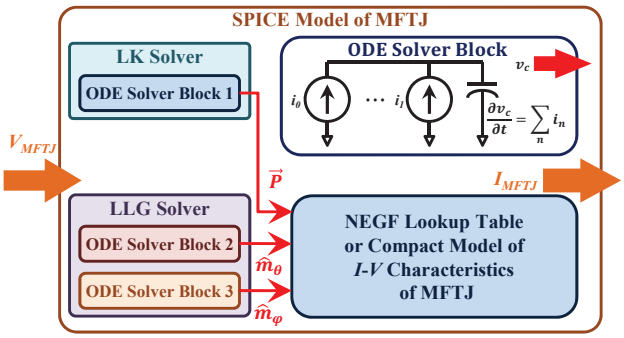

Fig. 3. Block diagram of our SPICE compatible MFTJ model.

We first write the MFTJ Hamiltonian, $\mathcal{H}$, as (9), where $\mathcal{H}_0$ and $\mathcal{H}_S$ are spin-independent and spin-dependent parts of $\mathcal{H}$, respectively. $\mathcal{H}_0$ may be written as in (14)-(16), where I is the 2×2 identity matrix, and N_L and N_R are the indices of the left and right interface lattice point, respectively (Fig. 2). $\hbar$ is the reduced Planck's constant, m_l^* is the effective electron mass in region l, and a is the uniform lattice spacing used for numerical calculation. The spin-dependent part is written as in (17), where $\vec{\sigma}$ represents the Pauli spin matrices, and $\hat{m}$ and Δ are the magnetization direction and the conduction band splitting of up-spins and down-spins at the lattice point, respectively. The barrier height of the tunnel barrier (U_B) is included in U_{OX} as in (18), while the voltage applied across the MFTJ (V_{MFTJ}) is modeled using U_{APP} as in (19). The effect of ferroelectric polarization in the tunneling barrier is modeled using (20)-(22), where δ_l and ϵ_l are the Thomas-Fermi screening length and relative permittivity of electrode l, respectively. Finally, the current density flowing through the MFTJ (J_{MFTJ}) can be calculated using (25). However, J_{MFTJ} depends on the relative angle between PL and FL (θ), and on the polarization of the ferroelectric tunnel barrier (P). In our model, the dependence of J_{MFTJ} on θ and on P are decoupled. Hence, for a fixed P, $J_{MFTJ}(\theta)$ may be calculated using (26), where $J_P = J_{MFTJ}(\theta = 0)$ and $J_{AP} = J_{MFTJ}(\theta = \pi)$. $J_{MFTJ}(P)$ may then be written as (27), where c_i are fitting parameters (different for $+P$ and for P) since P modulates the effective barrier height [4].

D. SPICE Compatible Dynamical MFTJ Model

The components of our SPICE compatible dynamical MFTJ model are shown in Fig. 3. The $I-V$ characteristics of the MFTJ returned by our NEGF solver are encapsulated as a compact model, and may also include $\overrightarrow{STT}$ calculated using (28)-(29) in the NEGF solver. Alternatively, the model for $\overrightarrow{STT}$ proposed in [8], written as (30)-(34), may also be used. Our SPICE model includes two blocks that allows SPICE to solve the LLG and LK equations during simulation of MFTJ based STT-MRAM memory cells. Each block consists of a capacitor network as shown in Fig. 3, where each current source represents one term in the differential equation and capacitor voltages are P and components of $\hat{m}$, in spherical coordinates in the LK and LLG block, respectively. P and $\hat{m}$ are used to calculate I_{MFTJ}, V_{MFTJ}, and $\overrightarrow{STT}$ during simulation.

TABLE I. EQUATIONS USED IN OUR PROPOSED SIMULATION FRAMEWORK

LLG: $\frac{\partial \hat{m}}{\partial t} = -|\gamma| \hat{m} \times \vec{H}_{EFF} + \alpha \hat{m} \times \frac{\partial \hat{m}}{\partial t} + \overrightarrow{STT}$ **(1)** $\vec{H}_{EFF} = \vec{H}_{UNI} + \vec{H}_{EXT} + \vec{H}_{DEMAG} + \vec{H}_{DIP} + \vec{H}_{TH}$ **(2)**

$\vec{H}_{DIP,j} = \sum_i \mu_r \frac{3\left(\frac{M_{S,i}}{M_{S,j}} \hat{m}_i \cdot \vec{r_i}\right)}{|\vec{r_i}|^6} \vec{r_i}$ **(3)** In-plane anisotropy: $\vec{H}_{UNI} + \vec{H}_{DEMAG} = \frac{2Ku_2}{M_S} \hat{m}_Z - 4\pi M_S \hat{m}_Y$ **(5)**

$\vec{H}_{TH} = \vec{\xi} \sqrt{\frac{2\alpha k_B T}{|\gamma| M_S V}}$ **(4)** Perpendicular anisotropy: $\vec{H}_{UNI} + \vec{H}_{DEMAG} = \left(\frac{2Ku_2}{M_S} - 4\pi M_S\right) \hat{m}_Z$ **(6)**

LK: $\frac{\partial \vec{P}}{\partial t} = -a_0 \frac{\partial F(\vec{P})}{\partial \vec{P}}$ **(7)** $F\left(\vec{P}\right) = F_0\left(\vec{P}\right) + a_1 \vec{E} \cdot \vec{P}$ **(8)**

NEGF: $\mathcal{H} = \mathcal{H}_0 + \mathcal{H}_S + U_{APP} + U_{FE} + U_{OX}$ **(9)** $t_l = \frac{\hbar^2}{2m_l^* a^2}$ **(10)** $t_l(k_\parallel) = \frac{\hbar^2 k_\parallel^2}{2m_l^*}$ **(11)** $\alpha_L = 2t_l + t_l(k_\parallel)$ **(12)** $\alpha_{INT,l} = 0.5(\alpha_{INT,l} + \alpha_{OX})$ **(13)**

$$\mathcal{H}_{0(i,i)} = \begin{cases} \alpha_L I & \text{if} \quad i < N_L \\ \alpha_{OX} I & \text{if} \quad N_L < i < N_R \\ \alpha_R I & \text{if} \quad i > N_R \\ \alpha_{INT,l} I & \text{if } i = N_L \text{ for } l = L, R \end{cases} \quad (14) \qquad \mathcal{H}_{0(i,i+1)} = \begin{cases} -t_L I & \text{if} \quad i < N_L \\ -t_{OX} I & \text{if } N_L \le i < N_R \\ -t_R I & \text{if} \quad i > N_R \end{cases} \quad (15)$$

$$\mathcal{H}_{0(i+1,i)} = \mathcal{H}^\dagger_{0(i,i+2)} \quad (16) \qquad \mathcal{H}_{S(i,i)} = 0.5\left(I - \vec{\sigma} \cdot \hat{m}\right) \Delta \quad (17)$$

$$U_{OX(i,i)} = \begin{cases} U_B I & \text{if} \quad N_L < i < N_R \\ 0.5 U_B I & \text{if} \quad i = N_L \text{ or } N_R \\ 0 & \text{else} \end{cases} \quad (18) \qquad U_{APP(i,i)} = \begin{cases} 0.5 V_{MFTJ} I & \text{if} \quad i \le N_L \\ -0.5 V_{MFTJ} I & \text{if} \quad i \ge N_R \\ \left(\frac{N_R - i}{N_R - N_L} - \frac{1}{2}\right) V_{MFTJ} I & \text{else} \end{cases} \quad (19)$$

$$U_{FE(i,i)} = \begin{cases} \sigma_S \phi_{L,i} I & \text{if} \quad i \le N_L \\ \sigma_S \phi_{R,i} I & \text{if} \quad i \ge N_R \\ \left(\frac{N_R - i}{N_R - N_L} - \frac{1}{2}\right) \sigma_S \left(\frac{\delta_L}{\epsilon_L} + \frac{\delta_R}{\epsilon_R}\right) I & \text{else} \end{cases} \quad (20) \qquad \phi_{l,i} = \frac{\delta_l e^{-|N_l - i|/\delta_l}}{\epsilon_l} \quad (21)$$

$|\sigma_S| = \left|\vec{P}\right|$, σ_S is positive if $\vec{P}$ is pointing left in Fig. 2 **(22)**

$G = [EI - \mathcal{H} - \Sigma_L - \Sigma_R]^{-1}$ **(23)** $\Gamma_l = i\left[\Sigma_l - \Sigma_l^\dagger\right]^{-1}$ **(24)** $J_{MFTJ} = \frac{q}{A_{MFTJ}\hbar} \int dE \, Tr\left[\Gamma_L G \Gamma_R G^\dagger\right](f_1 - f_2)$ **(25)**

$J_{MFTJ}(\theta) = J_P cos^2\left(\frac{\theta}{2}\right) + J_{AP} sin^2\left(\frac{\theta}{2}\right)$ **(26)** $J_{MFTJ}(\left|\vec{P}\right|) = e^{c_1|\vec{P}| + c_0}$ **(27)** $\overrightarrow{STT} = \frac{\mu_B}{M_S V} dV \vec{\nabla} \cdot \vec{J}_S$ **(28)**

$\left[\vec{\nabla} \cdot \vec{J}_S\right]_k = \frac{\int dE \, Tr\left[\sigma_k\left(\Sigma_b \mathcal{H}_{ab} G^n_{ba} - G^n_{ab} \mathcal{H}_{ba}\right)\right]}{i\hbar}$ **(29)** $\overrightarrow{STT} = \frac{|\gamma| g(\hat{m} \cdot \hat{p}) J_{MFTJ}}{2q\mu_0 M_S t_{FL}} (\hat{m} \times \hat{p} \times \hat{m})$ **(30)** $g(\hat{m} \cdot \hat{p}) = \left[\frac{q_+}{A_+ + A_-(\hat{m} \cdot \hat{p})} + \frac{q_-}{A_+ - A_-(\hat{m} \cdot \hat{p})}\right]$ **(31)**

$q_\pm = \left[P_{PL} \Lambda^2_{PL} \sqrt{\frac{\Lambda^2_{FL}+1}{\Lambda^2_{PL}+1}} \pm P_{FL} \Lambda^2_{FL} \sqrt{\frac{\Lambda^2_{PL}-1}{\Lambda^2_{FL}-1}}\right]$ **(32)** $A_\pm = \sqrt{\left(\Lambda^2_{FL} \pm 1\right)\left(\Lambda^2_{PL} \pm 1\right)}$ **(33)** $\Lambda^2 = \frac{A_{MTJ} q^2 k_F^2 R}{4\pi^2 \hbar}$ **(34)**

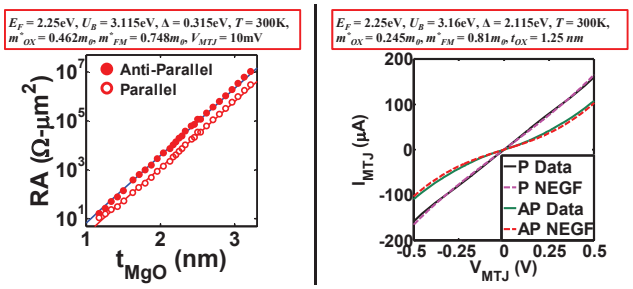

Fig. 4. Successful calibration of our NEGF solver to experimental data reported (left) in [9] and (right) in [5].

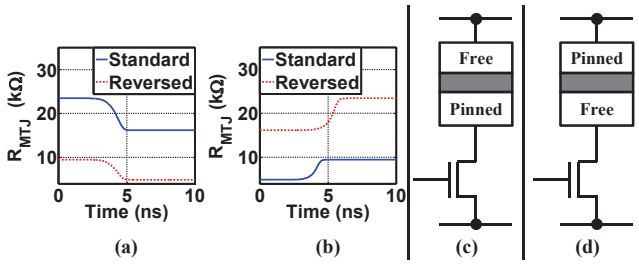

Fig. 5. Successful calibration of our SPICE model (without ferroelectric polarization) to experimental data reported in [10]. Worst case switching times for (a) Antiparallel to parallel and (b) parallel to antiparallel switching were 4.5ns and 5.5ns, respectively. The definition of (c) standard and (d) reversed cell connections are also shown.

E. Model Calibration

Our models are first calibrated to experimental data published in the literature before simulation. Since no experimental data on MFTJ is available (to the authors' best knowledge), our models were calibrated to MTJ measurements in [5], [9], [10] instead. Calibration results of our NEGF solver as shown in Fig. 4 shows our model and experimental data are in good agreement. Our LLG solver was calibrated to [10] as shown in Fig. 5. Results showed switching times between 4.5ns and 5.5ns, and are in good agreement with experimental data published in [10].

III. THE MULTIFERROIC TUNNEL JUNCTION (MFTJ)

The MFTJ structure (Fig. 6) consists of two ferromagnetic electrodes sandwiching an FTB. Ferromagnetic configuration of the MFTJ is switched using spin-transfer torque like in MTJ-based STT-MRAM. The current directions for anti-parallelizing (I_{AP}) and for parallelizing (I_P) the FL are shown in Fig. 6. Since the FTB is very thin, the electric field in the tunnel barrier during write operations may be sufficient to switch the FTB polarization when current is being passed through MFTJ to switch its FL magnetization. Hence, two configurations of ferroic properties exist in the structure as shown in Fig. 6. The remnant polarization in the FTB and non-zero screening lengths in the ferromagnetic electrodes result in a small *TER* effect as illustrated by the band diagrams in Fig. 2. The effective potential along the transport direction of the MFTJ is such that the barrier height is larger when FTB polarization points toward the electrode with the larger screening length. Although the *TER* effect is small when FTB is thin, it may be sufficient to enhance the *TMR* of the MFTJ and hence, reduce sensing failures in STT-MRAM.

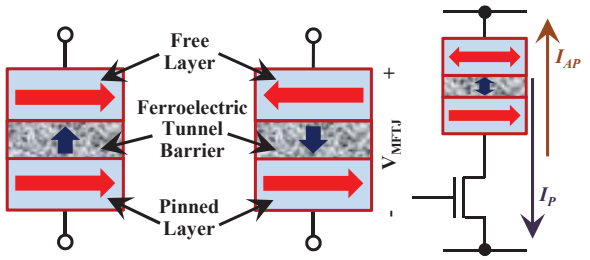

Fig. 6. The MFTJ structure consists of two ferromagnetic (FM) layers (blue with red arrows) sandwiching a thin ferroelectric layer (gray with dark blue arrows). The arrows denote the magnetization and electric polarization of the ferromagnetic and ferroelectric layers, respectively. In-plane anisotropy (IMA) FM layers are shown for illustration. The two memory states available are shown. (Right) The circuit schematic of the MFTJ based STT-MRAM memory cell with PL on the bottom. I_{AP} and I_P denote the current directions for anti-parallelizing and parallelizing the FM layers, respectively.

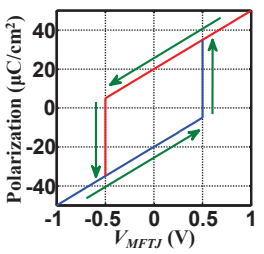

Gilbert Damping, α	0.014
Gyromagnetic Ratio, γ	17.6 MHz/Oe
Free Layer Geometry	50*nm*×50*nm*×1.4*nm*
t_{WRITE}, I_{C0}	5ns, 60μA
CMOS Technology	45*nm* bulk CMOS
Retention Barrier (E_A)	$56k_BT$
t_{OX}, Read V_{DD}, V_{READ}	1.25*nm*, 1.0V, 0.3V

Fig. 7. (Left) Ferroelectric polarization vs. applied voltage curve of MFTJ and (right) other simulation parameters (other than those in Fig. 4 used to calibrate our model to data in [5]) assumed in this work.

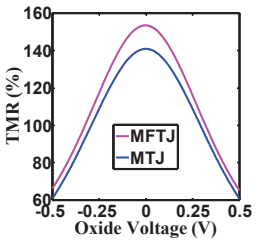

Fig. 8. Comparison of device TMR of MFTJ and MTJ.

IV. Simulation Results

We investigated an MFTJ by adding ferroelectic polarization to the MTJ from our calibration steps. The ferroelectric polarization versus electric field hysteresis curve and the ferromagnetic parameters assumed for the MFTJ are shown in Fig. 7 (t_{OX} in the MFTJ case is the equivalent MTJ t_{OX}). $\vec{P}$ is assumed to be pointing along the direction of electron transport. Device level *TMR* versus oxide voltage were calculated in our NEGF solver and plotted in Fig. 8, showing that the *TMR* of the MFTJ is 7.2% higher than that of the MTJ. However, the *TMR* of the MFTJ based STT-MRAM memory cell is only 4.7% higher than MTJ based STT-MRAM (assuming 900nm wide access transistor), implying that transistor resistance significantly affects *TMR* of the memory cell. Although the FTB enhanced the *TMR* of MFTJ based STT-MRAM, the overall resistance of the memory cell is also higher than that of MTJ based STT-MRAM. Consequently, read disturb current through the MFTJ based STT-MRAM is $0.3\mu A$ lower than in MTJ based STT-MRAM. Read disturb failures are thus lower in MFTJ based STT-MRAM than in MTJ based STT-MRAM. On the other hand, due to the larger resistance, MFTJ based STT-MRAM requires a write voltage of 0.973V compared to 0.971V in MTJ based STT-MRAM (considering 10% write margin, where write margin $= \frac{I_{WRITE}-I_{C0}}{I_{C0}} \times 100\%$).

V. Conclusion

We presented a hybrid spin-charge mixed-mode simulation framework for MFTJ based STT-MRAM. Our proposed simulation framework allows self-consistent solution of NEGF, LLG, and LK equations for SPICE simulation of STT-MRAM memory cells. Simulation results show that MFTJ based STT-MRAM memory cells can have slightly higher ($\sim 5\%$ higher *TMR* and lower read disturb failures as compared to MTJ based STT-MRAM memory cells. However, MFTJ based STT-MRAM memory cells require a higher write voltage as MFTJ resistance is higher compared to MTJ based STT-MRAM.

Acknowledgment

This work was supported in part by StarNET, a Semiconductor Research Corporation project sponsored by MARCO and DARPA, by the Semiconductor Research Corporation, and by Intel Corporation.

References

[1] Y. Huai, "Spin-Transfer Torque MRAM (STT-MRAM): Challenges and Prospects," *AAPPS Bulletin*, vol. 18, no. 6, pp. 33–40, 2008.

[2] X. Fong, S. H. Choday, and K. Roy, "Bit-Cell Level Optimization for Non-volatile Memories Using Magnetic Tunnel Junctions and Spin-Transfer Torque Switching," *IEEE Trans. on Nanotechnol.*, vol. 11, no. 1, pp. 172–181, Jan. 2012.

[3] X. Fong, Y. Kim, S. H. Choday, and K. Roy, "Failure Mitigation Techniques for 1T-1MTJ Spin-Transfer Torque MRAM Bit-cells," accepted for publication in *IEEE Trans. on Very Large Scale Integration (VLSI) Systems*.

[4] M. Y. Zhuravlev, Y. Wang, S. Maekawa, and E. Y. Tsymbal, "Tunneling Electroresistance in Ferroelectric Tunnel Junctions with a Composite Barrier," *Appl. Phys. Lett.*, vol. 95, no. 5, pp. 052902-1–052902-3, Aug. 2009.

[5] J. C. Sankey *et al.*, "Measurement of the Spin-Transfer-Torque Vector in Magnetic Tunnel Junctions," *Nature Physics*, vol. 4, no. 1, pp. 67–71, Jan. 2008.

[6] S. Sivasubramanian, A. Widom, and Y. Srivastava, "Equivalent Circuit and Simulations for the Landau-Khalatnikov Model of Ferroelectric Hysteresis." *IEEE Trans. Ultrasonics, Ferroelectrics, and Freq. Control*, vol. 50, no. 8, pp. 950–957, Aug. 2003.

[7] S. Salahuddin and S. Datta, "Self-consistent Simulation of Quantum Transport and Magnetization Dynamics in Spin-Torque Based Devices," *Appl. Phys. Lett.*, vol. 89, no. 15, pp. 153504-1–153504-3, Oct. 2006.

[8] J. Xiao, A. Zangwill, and M. Stiles, "Boltzmann Test of Slonczewskis Theory of Spin-Transfer Torque," *Phys. Rev. B* vol. 70, no. 17, pp. 172405-1–172405-4, Jul. 2004.

[9] S. Yuasa, T. Nagahama, A. Fukushima, Y. Suzuki, and K. Ando, "Giant Room-Temperature Magnetoresistance in Single-Crystal Fe/MgO/Fe Magnetic Tunnel Junctions." *Nature Materials* vol. 3, no. 12, pp. 868–871, Dec. 2004.

[10] T. Kishi *et al.*, "Lower-Current and Fast Switching of a Perpendicular TMR for High Speed and High Density Spin-Transfer-Torque MRAM," in *Proc. of 2008 IEEE Int. Electron Devices Meeting*, Dec. 2008, pp. 12.6.1–12.6.4.